



HAL
open science

Two-dimensional resonant magnetic soft X-ray scattering set-up for extreme sample environment

Stefan Stanescu, Cristian Mocuta, Frederic Merlet, Antoine Barbier

► **To cite this version:**

Stefan Stanescu, Cristian Mocuta, Frederic Merlet, Antoine Barbier. Two-dimensional resonant magnetic soft X-ray scattering set-up for extreme sample environment. *Journal of Synchrotron Radiation*, 2013, 20 (1), pp.181-189. 10.1107/S0909049512041325 . cea-01444153

HAL Id: cea-01444153

<https://cea.hal.science/cea-01444153>

Submitted on 23 Jan 2017

HAL is a multi-disciplinary open access archive for the deposit and dissemination of scientific research documents, whether they are published or not. The documents may come from teaching and research institutions in France or abroad, or from public or private research centers.

L'archive ouverte pluridisciplinaire **HAL**, est destinée au dépôt et à la diffusion de documents scientifiques de niveau recherche, publiés ou non, émanant des établissements d'enseignement et de recherche français ou étrangers, des laboratoires publics ou privés.

Two-dimensional resonant magnetic soft X-ray scattering set-up for extreme sample environment

Stefan Stanescu,^{a*} Cristian Mocuta,^a Frederic Merlet^b and Antoine Barbier^b

Received 3 April 2012

Accepted 2 October 2012

^aSynchrotron SOLEIL, l'Orme des Merisiers, BP 48, Saint Aubin, 91192 Gif sur Yvette, France, and^bCEA-Saclay/IRAMIS/ SPCSI, France. E-mail: stefan.stanescu@synchrotron-soleil.fr

The newly built MagSAXS (magnetic small-angle X-ray scattering) set-up dedicated to the direct two-dimensional measurement of magnetic scattering using polarized synchrotron radiation in extreme sample environments is presented. Pure optical transport of the image is used to record the magnetic scattering with a two-dimensional CCD visible-light camera. The set-up is able to probe magnetic correlation lengths from the micrometer down to the nanometer scale. A detailed layout is presented along with preliminary results obtained at several beamlines at Synchrotron SOLEIL. The presented examples underline the wide range of possible applications spanning from correlation lengths determination to Fourier transform holography.

© 2013 International Union of Crystallography
Printed in Singapore – all rights reserved

Keywords: resonant magnetic scattering; magnetic nanostructures; soft X-ray; diffraction; SAXS; Fourier transform holography.

1. Introduction

Innovation in materials science research requires optimized tools enabling access to new properties of matter. Successful advances and potential applications are likely to result from a balance between capabilities in fabricating novel artificial architectures and the ability to measure their useful properties. Although the advent of complex lithography processes (Saavedra *et al.*, 2010) has allowed a major step forward in fabricating genuine architectures, researchers still lack access to suitable tools addressing the emerging behaviors (collective phenomena) like correlations in assemblies of nanostructures or self-assembled nanostructures. In such architectures interesting electronic and magnetic properties are governed by correlation factors at nanometer length scales. However, only a very few techniques are available nowadays that allow a direct statistical approach for quantifying such fundamental behaviors. The magnetic and/or electrical domain structures are of high interest in current research and correspond to typical ordering resulting from the degree of correlation (Skuza *et al.*, 2010; Eerenstein *et al.*, 2006; Moubah *et al.*, 2012; Seemann *et al.*, 2012).

Synchrotron radiation small-angle X-ray scattering (SAXS) is a promising approach in order to tackle this issue because through wavelength tuning it can be made highly element sensitive and relevant to the interesting nanometer length scales. In a previous work the hard X-ray regime has been explored using MASAXS (magnetic anomalous SAXS) at the Fe *K*-edge and Gd *L*_{3,2}-edges (Fischer *et al.*, 1997). To the best of our knowledge it is the only report dealing with high-energy SAXS experiments in a magnetic contrast mode. The authors clearly demonstrated the experimental feasibility and, more

importantly, presented new insights into the magnetic properties directly related to the granular character of the studied system. Tuning the energy of the X-ray beam to the soft regime allows probing the resonant response in the energy range of the 3*d* transition metals absorption edges (500–1000 eV) with enhanced sensitivity to their magnetic properties [soft X-ray resonant magnetic scattering; see, for example, van der Laan (2008)]. The pioneering work of Kortright and co-workers (Kortright *et al.*, 2001*a,b*; Hellwig *et al.*, 2002) demonstrated the feasibility of resonant SAXS measurements in the soft X-ray regime. Their approach showed the high chemical sensitivity and a suitable spatial resolution applied to heterogeneous magnetic films. The study of extended regions of the reciprocal space was, however, not reported.

The MagSAXS (magnetic small-angle X-ray scattering) set-up presented here consists of a reflection geometry under critical or sub-critical incidence conditions. Thus the surface sensitivity is enhanced in addition to high element and magnetic sensitivity. This approach could be understood as a GISAXS (grazing-incidence SAXS) set-up optimized for the soft X-ray regime. It has the great advantage of avoiding specific sample preparation like in a transmission geometry. Although the examples hereafter detail only the reflection geometry, we should point out that this set-up is also well suited for transmission geometry, most of the time associated with SAXS experiments. While the general GISAXS principles for the hard X-rays are well established (Renaud *et al.*, 2009), there are some notable differences related to the use of soft X-rays as a probe. Firstly, the incident and scattering angles are much larger than those corresponding to the high-energy X-rays. Typically, grazing geometry for hard X-rays involves an incident angle close to the critical angle for total

external reflection (0.1°). They translate here into angles of several degrees. This applies for the scattering angles too, which are also of several degrees (see §2.1). Secondly, the use of soft X-rays results in a Ewald sphere of much smaller radius compared with the hard-energy X-ray regime. When an area detector is used, converting the recorded signal into the reciprocal space yields a curved surface. For hard X-rays the area detector image is directly approximated to a planar cut in the reciprocal space. This approximation no longer works for soft X-rays. Consequently, features in reciprocal space like satellites, facets or rods will now appear more like one-dimensional signals such as spots or regions of rods.

2. Experimental set-up

The aim of the present work was to build a set-up and demonstrate its utility in performing magnetic resonant scattering in the soft X-ray regime for extreme sample conditions, *i.e.* very high magnetic fields (up to 7 T) and very low temperatures (down to 1.5 K). Importantly, such sample environments are typical for magnetic X-ray dichroic measurements since combining low temperature and high field allows magnetic anisotropies and thermal fluctuations to be overcome. Up to now, for the different magnetic scattering studies, previous authors reported either downgraded detection conditions using more often zero- or one-dimensional detectors (Dürr *et al.*, 1999; Kortright *et al.*, 2001a) or mild sample environments (Miguel *et al.*, 2006, 2007; Peters *et al.*, 2004) in order to ensure the practical feasibility of the experiments. In the high X-ray energy range, small-angle scattering experiments have typical detector-to-sample distances, L , of several meters, making harsh sample environment (Bras, 2007) set-ups easier to build, even if one has to deal with long sections under vacuum and very large detectors. In the soft X-ray regime the working distance is of only several centimeters and therefore it is the most constraining parameter limiting possible measurements. Moreover, tuning this working distance is crucial since it allows a wide range of magnetic correlation lengths to be probed ranging from the nanometer to micrometer scales (as we will see in Fig. 1). The MagSAXS set-up was designed by taking into account exclusively the constraints of a typical magnetic dichroism set-up such as on the DEIMOS (Dichroism Experimental Installation for Magneto-Optical Spectroscopy) beamline (see §2.1). However, it is flexible and simple enough to allow its implementation on any synchrotron beamline be it soft or hard X-ray energy.

2.1. General considerations

The geometry described in Fig. 1(a) shows the detector (scintillator screen) mounted at a distance L downstream of the sample, with k_i being the incidence wavevector and k_f the scattered wavevector. In the specular case the emergent angle is equal to the incidence angle and the angular momentum transfer can be written as $q = (4\pi/\lambda)\sin\theta$, with λ being the X-ray wavelength and 2θ the scattering angle. In the following

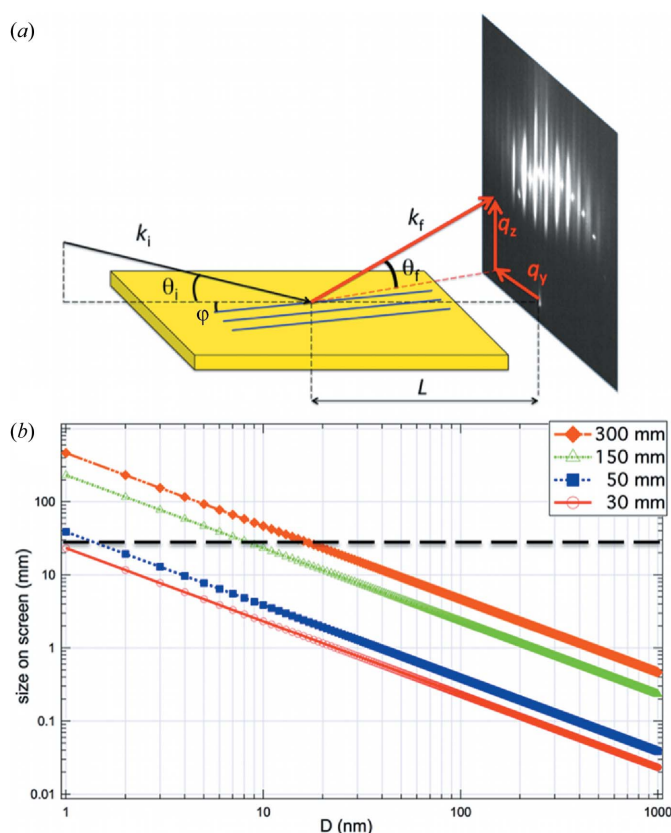


Figure 1
 (a) Scattering geometry and notations: k_i and k_f are the incident and emergent wavevectors, respectively, θ_i and θ_f are the incident and emergent scattering angles, ϕ is the azimuthal angle, q_z and q_y are the momentum transfer along the z and y directions, respectively, L is the distance between the sample and the scintillator screen. (b) Characteristic lengths in the angular space (s in the text) as a function of the object characteristic sizes/spacings in the direct space, D . The graphs are plotted for four different L values: 30, 50, 150 and 300 mm. Objects from a few tens of nanometers up to a few micrometers can be measured by simply adjusting the sample-to-screen (YAG) distance. The dashed line at $y = 17.8$ mm corresponds to the field of view of the MagSAXS set-up.

an estimation of the characteristics of this set-up and its performances are given. If D is the characteristic correlation length, expressed in nanometers, describing the objects on the sample surface, then the corresponding momentum transfer is given by $q = 2\pi/D$. From simple geometric considerations the scattered spot on the scintillator screen will have an angular spread of $\sin\theta = s/L$, where L denotes the sample-to-screen distance and s is the size of the scattered spot on the screen. Therefore one can write $2\pi/D = (4\pi/\lambda)s/L$, or $s = (1/D)L\lambda/2$. In Fig. 1(b) we show the dependence of the characteristic signal size on the screen, s , as a function of the correlation length D characteristic of the sample, for four different sample-to-scintillator screen distances. From this representation we derive that for measuring micrometer-scale magnetic correlations one has to set L to large values to avoid being limited by the pixel resolution of the detector. As an example, if $L = 30$ mm, for D larger than $1\ \mu\text{m}$, the pixel resolution will fall below $10\ \mu\text{m}$. When probing nanometer-scale features, low values for L are needed in order to scatter inside the detector's field of view. The horizontal dashed line in Fig. 1(b)

at $y = 17.8$ mm corresponds to the chosen field of view of the MagSAXS set-up. Hence one can conclude that we need a detection system with a relatively small pixel size in conjunction with a tunable sample-to-screen distance. Without any other constraints, the optical and geometrical criteria alone could be easily satisfied when choosing the detection system.

Quantitative measurements, at the atomic scale, in the field of magnetism, generally require high applied magnetic fields and low temperatures. It appears thus obviously that the MagSAXS detection system has to fit in a heavy dedicated sample environment, e.g. an ultra-high-vacuum superconducting magnet used for magnetic circular and linear dichroism measurements. Therefore, the MagSAXS set-up design was optimized and tested on the DEIMOS beamline at Synchrotron SOLEIL, France, which offers a superconducting magnet characterized by high magnetic fields, 7 T and 2 T, orthogonal in the transverse beamline plane, along with very low sample temperatures, down to 1.5 K. Fig. 2 shows the DEIMOS superconducting magnet, together with its environment: UHV dedicated for *in situ* sample preparation and analysis (evaporation sources, ion etching, Auger electron spectroscopy, low-energy electron diffraction, scanning tunneling microscopy), and a sample transfer glove-box which allows direct access to the UHV environment without any contamination for fragile samples, especially hydrophobic chemical species. As can be observed in Fig. 2(a), the

MagSAXS set-up fits perfectly in this dense surroundings. In Fig. 2(b) we present a closer view showing the CCD camera along with its mount and optical video-microscope, placed on the linear, 300 mm stroke, motorized manipulator. Figs. 2(c) and 2(d) present sketches of the MagSAXS set-up as implemented on the DEIMOS end-station, as a top view and side view, respectively. We stress the very limited access inside the superconducting magnet, as well as the mounting of the sample placed at the end of the long cold finger. Furthermore, this sketch allows us to easily highlight the elements added to the standard DEIMOS end-station: the CCD camera with its optics and the YAG:Ce scintillator crystal along with its UHV support.

For the measurements, the sample is mounted in a vertical geometry on the long cold finger provided with vertical motion and polar rotation, used to set the incidence angle in the MagSAXS set-up. Moreover, the superconducting magnet itself is mounted on a motorized table allowing positioning in the vertical and horizontal perpendicular to the beam directions. We can overcome the limiting motors parameters (accuracy, reproducibility, etc.) since we are using a fixed geometry, like in a GISAXS experiment. In all cases the motorized movements were good enough for sample alignment.

The following paragraph provides a brief overview of the DEIMOS beamline. An exhaustive beamline report is beyond the scope of the present paper, even though a short presentation

is of crucial interest in order to understand the MagSAXS set-up context, as being a part of the end-station set-up. The beamline is optimized for magneto-optical spectroscopies (circular and linear X-ray magnetic dichroism) in the soft X-ray energy range (300–2500 eV) covering the *3d* transition metals and *4f* rare-earth absorption edges, with optics insuring very high stability and spectral purity. The X-ray source is an Apple II undulator that supplies high rates ($\sim 100\%$) for circular and linear polarizations. A high-resolution monochromator ($E/\Delta E > 10^4$) delivers a relatively high flux on the sample, $\sim 6 \times 10^{12}$ photons s^{-1} (0.1% bandwidth) $^{-1}$ at 750 eV, in a beam spot of $\sim 80 \mu\text{m} \times 80 \mu\text{m}$ size at the sample position. Dichroic spectra are derived from the difference between two configurations between the polarization of the incoming beam and the applied magnetic field. The high stability of the beamline is obtained by downgrading the monochromator resolving power to values of $E/\Delta E \simeq 5000$ –6000, by using higher values of the exit slits gap (for example, with a 100 μm exit slit gap the

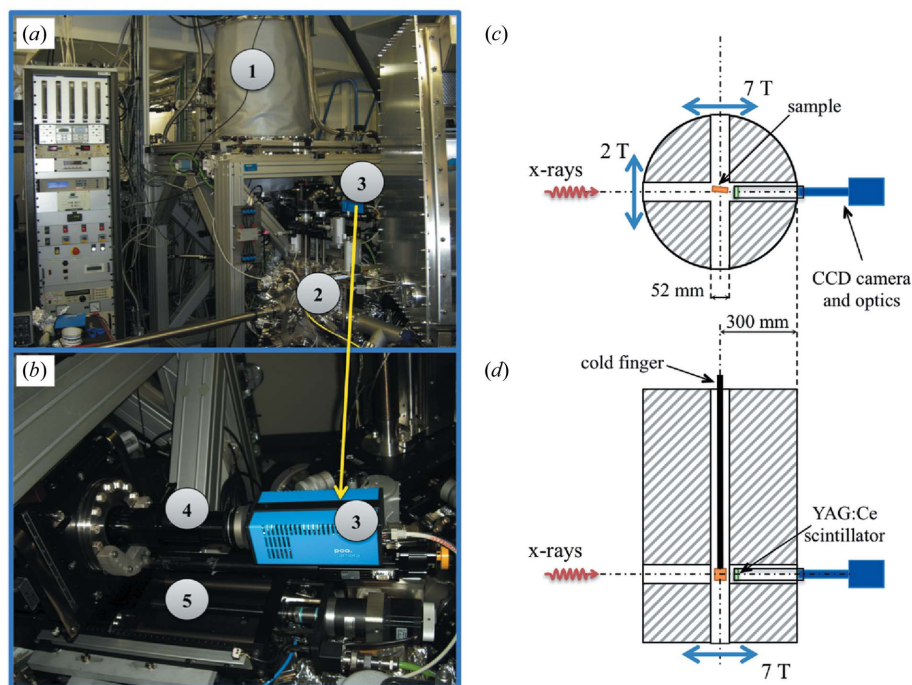


Figure 2

Experimental set-up on the DEIMOS beamline. (a) 1, superconducting split coil magnet (7 T + 2 T), the sample is located inside the magnet with $T = 1.5$ –370 K; 2, one of the UHV chambers dedicated to *in situ* sample preparation and analysis; 3, CCD camera. (b) Zoom on the MagSAXS set-up: 3, CCD camera; 4, optical video-microscope; 5, the 300 mm translation. (c) and (d) Schematic top- and side-views, respectively, of the MagSAXS set-up as used on the DEIMOS superconducting magnet. We emphasize the sample position, situated in the center of the superconducting magnet cold bore, supported by the cold finger [the black rod in (d)].

resulting resolution at 750 eV is 0.15 eV). In order to match the MagSAXS design with the existing end-station, we had to consider several limitations:

(i) Limited access: the split coil geometry has 52 mm-diameter inner tubes of length 300 mm, as shown in Figs. 2(c) and 2(d); this constitutes the access path both for impinging and scattered X-ray beams, thus also for the detector.

(ii) Very high magnetic fields: materials have to be non-magnetic and they should not influence the homogeneity of the magnetic field inside the bore. Moreover, an electron-based detection probe would be hampered by the magnetic field. Hence an optical detection and image transport was preferred.

(iii) Very high temperature gradients: the sample can be maintained at 1.5 K and the surrounding tubes are at liquid-He temperature, *i.e.* 4.2 K. Any inclusion of elements conducting the 300 K from outside the magnet would boil the liquid He in the reservoir.

(iv) Since we are dealing with soft X-rays, sample and detector have to be inside the UHV environment.

2.2. Materials and design

To overcome all these constraints several choices had to be made concerning the optical layout and the mechanical and/or material supports. First of all, it is obvious that obtaining a scattering image corresponding to nanometer-scale objects imposes a very short sample-to-screen distance and a large field of view, as discussed above. Since the space available is very limited inside the superconducting magnet and considering the high magnetic field and low temperatures, a YAG doped with Ce (CRYTUR, 2012) scintillator was considered as a suitable solution. Fig. 3 shows, in the lower panel, a close view of the internal (UHV) parts of the set-up, as used on the METROLOGIE beamline at Synchrotron SOLEIL, during early tests. The 40 mm-diameter and 0.5 mm-thick scintillator is mounted on a polyether ether-ketone (PEEK) tube. PEEK is UHV-compatible and can handle the huge thermal gradient, from room temperature down to 4.2 K within the size of our set-up. The scintillator is not tightened, but kept in place through small lateral PEEK screws, in order to avoid any induced mechanical strain that could appear upon strong temperature changes. This PEEK tube is rigidly fixed on a stainless-steel ring that also serves as support for the special fused-silica viewport (high transmission rate of $\sim 95\%$ for visible light), at the UHV–air interface. Both the viewport and YAG:Ce scintillator are anti-reflection coated, ensuring very high transmission rates at the 550 nm characteristic emission line of the scintillator. As can be observed in Fig. 3(a), this UHV part is inserted into an XYZ manipulator, with a linear stroke along the *X* direction of 300 mm, ensuring a tunable sample-to-screen distance to cover the range depicted in Fig. 1(b). Having a 300 mm stroke allows us to set the scintillator at the sample position and therefore fully characterize the beam shape and size. A CCD 14-bit PCO2000 (PCO2000, 2012) camera (see Fig. 2) is used to image the scintillator, through a specially designed video-microscope objective

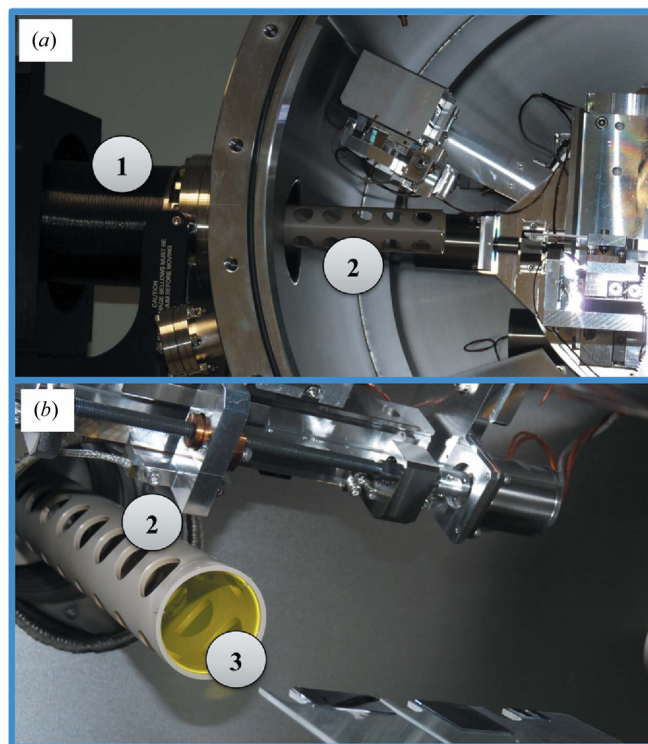


Figure 3

Detailed *in situ* view of the MagSAXS set-up (photograph corresponding to the set-up on the METROLOGIE beamline, inside the in-vacuum reflectometer): (a) 1, three-axes manipulator with a linear stroke of 300 mm; 2, PEEK support. (b) View from the beam direction: 2, PEEK support; 3, YAG:Ce scintillator crystal.

(Optique Peter, 2012). Thus, the overall optical parameters of the detection system are: a pixel size of $8.7\ \mu\text{m}$ combined with a fixed camera–YAG scintillator of 365 mm. The resulting field of view for 2048×2048 pixels is thus $17.8\ \text{mm} \times 17.8\ \text{mm}$. The set-up also allows, by means of changing the mount of the CCD camera, different CCD-to-YAG scintillator distances to be set. For example, if a larger field of view is needed, with an increased pixel size, the video-microscope can work at 580 mm for a resulting pixel size of $14.2\ \mu\text{m}$ and a field of view of $29.1\ \text{mm} \times 29.1\ \text{mm}$.

2.3. Advantages and limitations

Importantly, even if the MagSAXS set-up has been optimized for extreme sample environments, it can be adapted to any synchrotron beamline, be it soft or hard X-ray regimes. Unlike direct (or back) illuminated CCD (Beutier *et al.*, 2007, 2008) cameras, fast-readout and fast-shutter systems that protect burning out of the CCD chip are here not necessary. The use of the MagSAXS set-up is thus more comfortable and does not need special care. When installed on a soft X-ray beamline, the YAG:Ce itself absorbs the beam completely protecting the sensitive part of the CCD. Therefore, overexposure of the detection system can be used, without damage, during the alignment phase when direct and reflected beam are recorded. Moreover, we can artificially increase the 14-bits dynamical range of the camera using different expo-

sure times, the lower signal being optimized by overexposing the stronger features of the scattered image. This specificity implies an intrinsic limitation. Longer exposure times or acquisition of many frames for summation, compared with directly illuminated CCD cameras, are needed to obtain the same information. Directly illuminated CCD cameras are expected to be far more sensitive with higher signal-to-noise ratios. However, as will be shown in this paper, the MagSAXS set-up can be used as a ‘safe option’ for the expensive directly illuminated CCD cameras for a number of experiments. The set-up was also tested on a hard X-ray beamline in order to perform standard GISAXS measurements.

The following section of the paper will describe several types of measurements: (i) a magnetic resonant scattering experiment performed at the DEIMOS beamline of Synchrotron SOLEIL; (ii) results from the same sample measured on a hard X-ray beamline (namely the DIFFABS beamline at SOLEIL) in a GISAXS geometry, and (iii) some insight will be given concerning the use of the MagSAXS set-up implemented at the SEXTANTS beamline at Synchrotron SOLEIL in a very sensitive detection mode, *i.e.* Fourier transform holography.

3. Example of measurements

3.1. Resonant magnetic scattering on a periodic magnetic grating

The sample is mounted vertically and a half-cut procedure following iterative scans of the sample lateral position and incidence angle is used to align the sample at zero incidence in the direct beam. The geometry of the superconducting magnet is such that the sample is located at the center of rotation, coinciding with the center of the cold bore, where the inhomogeneity of the magnetic field is lower than $1\% \text{ cm}^{-3}$. For magnetic measurements this value is crucial since it guarantees a homogeneous orientation of the magnetization inside the sample. In the absence of a homogeneous magnetic field, the measured dichroic signal would be reduced nonlinearly compared with the real value corresponding to the perfect alignment between the applied magnetic field and the polarization vector of the incident photon beam. Once the sample is aligned with respect to the direct beam, several incidence angles are tested, for different L values, in order to optimize the scattered signal recorded from the YAG:Ce scintillator crystal. We have to note here that owing to geometric and field of view constraints all measurements are carried out for incidence angles below the critical ones. Measuring above the critical angle would oblige us to reduce L consequently. We will thus be limited by the detector pixel resolution and lose the benefit of the large field of view. One can use an additional adapted magnification optics to overcome the pixel size constraint, but it would be of limited interest for the experiments we are interested in.

Our first test sample was a grating consisting of periodic Co lines with $\Lambda = 300 \text{ nm}$ spacing. It was elaborated using a nanoimprint technology, first presented by Chou *et al.*

(1996), from a layered thin film structure of Ta(5 nm)/Co(20 nm)/Ru(5 nm) deposited on a Si(100) substrate. Using this kind of lithographic process ensures large area samples are obtained, which is important when dealing with grazing-incidence measurement geometry. Fig. 4(a) shows an optical microscopy image of the sample. From this image we note that the sample shows several imperfections (line defects). Some domains thus appear to be shifted by half a period. Fig. 4(b) presents a SEM (scanning electron microscopy) image recorded on a defect region of the sample. The contrast occurs between alternate Co lines (bright regions) and etched Si substrate (dark regions). First, we can easily notice the absence of regular Co lines with fixed 300 nm width. Instead, alternate wide and narrow Co lines appear. Second, like in the highlighted area, we observe modulations in the lines width. Such modulations define the boundaries of the shifted domains appearing in the optical image (Fig. 4a). Most probably, during the nanoimprinting process, the lines were not transferred perfectly from the mask to the resist, owing to variation in processing parameters such as the pressure and the temperature. Therefore many defects occur prior to the sputtering of the metallic layers. As a direct consequence, in the scattered images we can identify two different scattered signal families, as shown in Fig. 4(c): the first, at $q_y = 4.72 \times 10^{-4} \text{ nm}^{-1}$, corresponds to a periodicity of $\sim 266 \text{ nm}$, while the

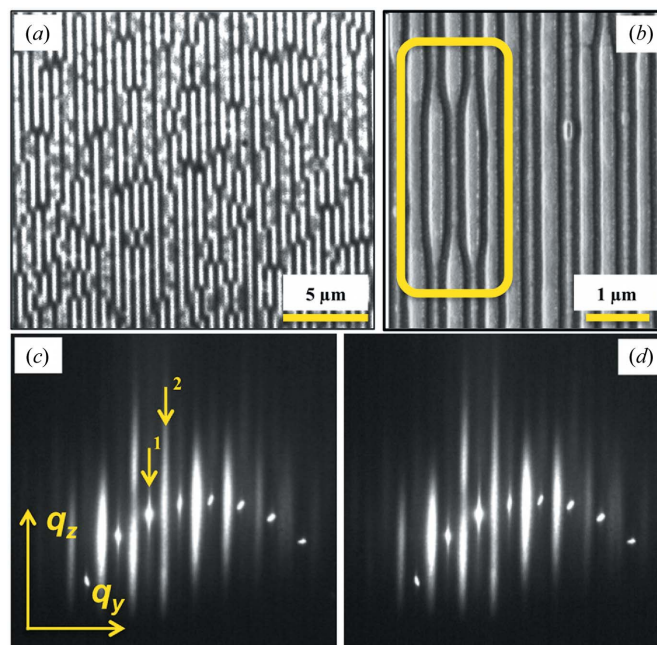


Figure 4

(a) Co lines obtained by nanoimprint with a periodicity of $\sim 300 \text{ nm}$. (b) Detail in SEM showing the defects in the nanoimprint process. The contrast occurs between alternate Co lines (bright lines) and clean Si substrate regions (dark lines); (c) and (d) Raw CCD images as recorded under an applied magnetic field of +2 T, at 772.1 eV using circular right ($\sigma+$) and circular left ($\sigma-$) helicities, respectively: 1, specular and diffraction orders arising from the regular grating; 2, half-order contributions coming from the double period. Images, recorded with a 3 s exposure time, are shown on a log scale to optimize the rendering. Only about a quarter of the entire field of view of the camera is shown.

second, at $q_y/2$, occurs from the double period (2Λ) and is much more diffuse both in the q_y (or q_{\parallel}) and q_z (or q_{\perp}) directions. The q_y spreading can be understood as related to a poorly organized double-period structure, owing to the dispersion of domains with double-period defects. On the contrary, the q_z spreading is not so obvious and deserves further discussions. We follow an argument similar to that of Yan & Gibaud (2007) for the hard X-ray regime. In a surface-scattering experiment the spots recorded on the detector's screen occur as the projection of the intersection between the surface truncation rods with the Ewald sphere. At high X-ray energies the detector screen can be assimilated directly with the Ewald sphere owing to its small curvature. The diffuse-scattering features coming from the sample surface are thus considered to intersect the detector directly and the spreading in the transfer momentum can be directly measured on the screen. On the contrary, at low X-ray energies the curvature of the Ewald sphere is very large and this approximation fails. The recorded spots exhibit an amplified spreading given by the projection of the rod–Ewald-sphere intersection on the detector plane, as described in the following. If we consider $d\omega$ as the arc on the Ewald sphere describing its crossing with a scattering feature along q_z , the projected size, s , on the YAG:Ce screen will be given by $s = L/[k \cos^2(2\theta)] d\omega$, where k is the wavelength (defining the Ewald sphere radius, $k = 2\pi/\lambda$), L is the sample-to-YAG scintillator distance, and 2θ is the scattering angle. While the q_z momentum transfer describes interferences along the perpendicular to the sample direction, q_x is the result of interferences along the beam propagation direction in the sample plane. In the case of hard X-rays (20 keV, for example), where in a typical GISAXS measurement the screen is considered in a first approximation to be indistinguishable from the Ewald sphere (small curvature), we obtain a value of $k = 2\pi/\lambda = 1.014 \text{ nm}^{-1}$, while, at 800 eV, $k = 0.0405 \text{ nm}^{-1}$. It is therefore straightforward to make a comparison between hard and soft X-ray conditions. If L and $d\omega$ are constant, the spreading observed in the soft X-ray case owing to the Ewald sphere curvature will be $1.014/0.0405 \simeq 25$ times larger. Additionally, another Ewald sphere curvature effect is that the apparent q_z will be in fact a mixture of q_z and q_x components. In the present case, from the optical images we can estimate a mean domain size along the beam of about 550 nm giving therefore only a small contribution of the q_x component. The very large spreading of q_z is therefore mostly related to the form factor of the film thickness, of about 20 nm.

The sample was aligned at a fixed incidence angle of 2.3° , and the sample-to-screen distance was set at 150 mm. These values were found to give the optimized scattering images, *i.e.* to cover the highest possible reciprocal space with the detector's field of view. Two scattering images, shown in Figs. 4(c) and 4(d), are chosen at the maximum of the Co L_3 resonance, *i.e.* 772.1 eV. Complete energy scans in the 750–810 eV range covering the Co $L_{3,2}$ absorption edges for two configurations of the helicity of the circular polarization ($\sigma+$ and $\sigma-$, respectively) and the applied magnetic field ($H+$) were recorded. As can be easily noticed from both images, they are not perfectly symmetric, owing to an azimuthal misalignment

(see also Yan & Gibaud, 2007) during sample mounting. Unfortunately the superconducting magnet cold finger does not provide an azimuthal rotation and therefore special care has to be taken while mounting the sample. This strong misalignment effect will be detailed later (see §3.2). To eliminate any experimental artifacts from the dichroic signal, a full set of field/polarization configurations was used, *i.e.* $\sigma + H+$, $\sigma - H+$, $\sigma + H-$ and $\sigma - H-$. The resulting signal, presented in Fig. 5(a), for an energy corresponding to the Co L_3 resonance, was obtained as $(I^{\sigma+H+} - I^{\sigma+H-}) + (I^{\sigma-H-} - I^{\sigma-H+})$. It is important to note that this difference image is obtained directly by subtracting the circular right and left helicities corresponding images, without any additional image processing. We can index the different scattering orders as shown in Fig. 5(a), starting from the specular as zero, with $q_y = n \times 4.72 \times 10^{-4} \text{ nm}^{-1}$. The integer indexed diffracted spots correspond, as already discussed above, to the 300 nm Co line period, while the $n/2$ orders yield from the double-period domains. No peaks appear characterizing an antiferromagnetic alignment between the lines, as observed for example in dipolar coupled perpendicularly magnetized Co/Pt nano lines (Chesnel *et al.*, 2002). In that case, the dipolar

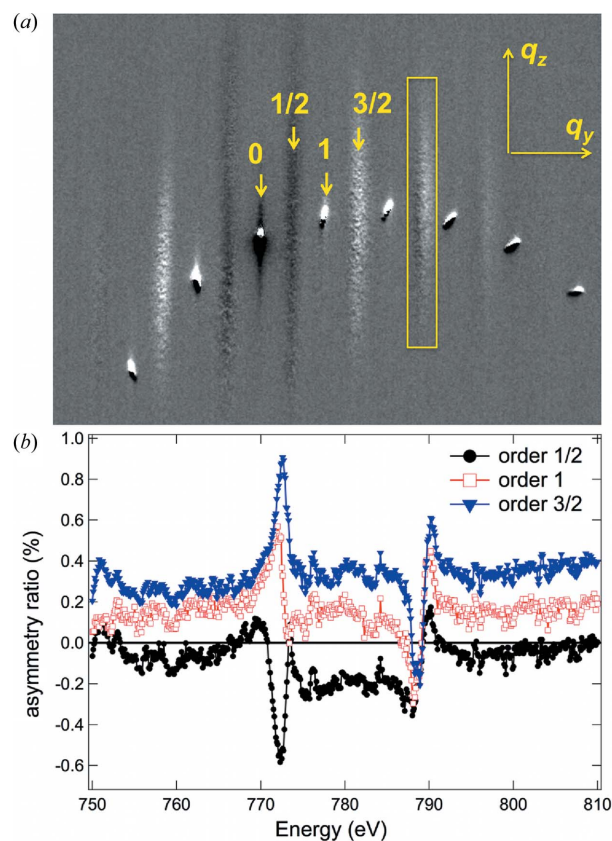


Figure 5 (a) Scattering contrast image obtained as the difference between circular right and circular left helicities of the incoming light, for a given applied external magnetic field direction. The diffraction orders are labeled starting from the specular equal to 0. The rectangle shows the region of interest used for integrations in order to obtain (b) asymmetry ratios $(I^+ - I^-)/(I^+ + I^-)$ expressed in % for the 1/2, 1 and 3/2 orders as a function of energy. For clarity the 1 and 3/2 orders were shifted by 0.2% and 0.4%, respectively.

interaction between the lines with an interline gap smaller than 200 nm was shown to favor antiparallel alignment between the lines magnetization. Thus, in our case, the magnetic contrast occurs only because of a ferromagnetic ordering between the lines and is therefore superposed on the grating charge scattering. In order to better illustrate the magnetic contribution, we report in Fig. 5(b) the asymmetry ratio (Kao *et al.*, 1990, 1994; Tonnerre *et al.*, 1995), $R_a = (I^+ - I^-)/(I^+ + I^-)$, of the indexed scattering orders, where I^+ denotes the parallel (*i.e.* $I^{\sigma+H+}$ and $I^{\sigma-H-}$) and I^- the antiparallel (*i.e.* $I^{\sigma+H-}$ and $I^{\sigma-H+}$) configurations. For that purpose the indexed orders are integrated on a defined region of interest (ROI), *i.e.* the rectangular frame in Fig. 5(a). It is important to note that this ROI corresponds to the typical acceptance when using silicone diode detectors to integrate diffuse magnetic scattering (Dürr *et al.*, 1999; Spezzani *et al.*, 2004). Magnetic contrast is easily identified and reversed behavior can be noticed between the 1/2, 1 and 3/2 scattering orders. For clarity, the curves corresponding to the 1 and 3/2 orders were shifted vertically by 0.2% and 0.4%, respectively. As explained above, the defects induced during the nano-imprinting process and yielding the $n/2$ interferences are probably at the origin of the reversed magnetic behavior. Indeed, at first glance, we can speculate on the reversed magnetization orientation of these domains with respect to non-disturbed ones, resulting in a reversed R_a . In any case, a full description of the magnetic behavior can be made only by deducing the terms involved in the total scattering factor [see, for example, Tonnerre *et al.* (1995) and Chesnel *et al.* (2002)]. Such calculations/analysis are, however, well beyond the purpose of the present paper.

All signals were normalized with respect to a monitor signal, I_0 , collected from the Wolter-type focusing mirror of the beamline. Using a good normalization is crucial since in the magnetic scattering the signal measured is very small and therefore often hidden by strong direct beam fluctuations. For magneto-optical spectroscopies in the soft X-ray range, the incident monitor, I_0 , is insured by the absorption on a gold mesh, with typical absorption coefficients above 50%. In this way the majority of the incoming photons are used for the I_0 signal, allowing very high sensitivity (Brune & Gambardella, 2009). This usual method of normalization is unsuitable here because a parasitic scattered signal appears in the recorded images originating from the X-ray diffraction on the gold mesh. We describe here a possible way to normalize the recorded data. Prior to the MagSAXS energy scan, we have to record both $I_0^{\text{mir}0}(E)$ from the mirror and $I_0^{\text{mesh}}(E)$ from the gold mesh inserted in the direct beam, obtaining thus the ratio $R(E) = I_0^{\text{mir}0}(E)/I_0^{\text{mesh}}(E)$. During the MagSAXS measurement we record $I_0^{\text{mirMAG}}(E)$ from the mirror and $I_{\text{img}}(E)$ from the scattered image. Therefore the normalized scattered signal will be $I_{\text{img}}^{\text{norm}}(E) = I_{\text{img}}(E)/[I_0^{\text{mirMAG}}(E)R(E)]$. The small noise increase in Fig. 5 is due to the less accurate normalization with respect to the incident beam. Unfortunately the measurements presented in Fig. 5 have not been processed using this new normalization method, since only $I_0^{\text{mirMAG}}(E)$ could be recorded during the tests.

3.2. Hard X-ray GISAXS: complementarity to soft X-ray studies

The MagSAXS set-up was successfully tested in a high-energy X-ray GISAXS configuration on the DIFFABS beamline at Synchrotron SOLEIL. We measured the same nanoimprinted sample as described above in a standard high-energy X-ray GISAXS geometry (Renaud *et al.*, 2009). The photon energy was set at 7.5 keV, the incidence angle on the sample at 0.45° and the sample-to-YAG scintillator distance, $L = 1200$ mm. Fig. 6 shows the GISAXS pattern obtained for different azimuthal angles φ . Similar to the soft X-rays, the GISAXS patterns present two different scattering families, integer and half orders. Their origin is explained in a similar way to the soft X-ray measurement case. The sharp and intense spots originate from the periodic gratings aligned approximately along the incident X-ray beam. The sample behaves like a rather well ordered system, resulting in a scattered signal in reciprocal space exhibiting sharp features. In this case, even if high-energy X-rays are used, the slight curvature of the area detector in the reciprocal space can be observed. The above-mentioned sharp signal does not yield vertical rods but sharp spots, with positions depending on the relative orientation of the grating with respect to the incident X-ray beam (*i.e.* sample azimuth). This behavior can be fully modeled and understood (Yan & Gibaud, 2007).

The second-order satellites originating from the double-period areas exhibit a broad rod-like feature in the q_z direction. These double-period areas of the sample show a poor organization. The corresponding scattering signal is expected to be broader in reciprocal space in all directions. Consequently, the interception of this signal by the detector will result (both for hard and soft X-rays) in a signal having a more important extension in the q_z direction (see discussion in §3.1).

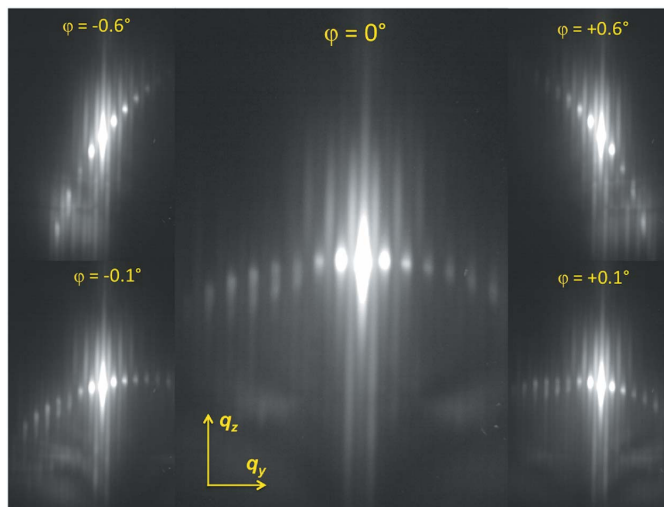


Figure 6 GISAXS patterns recorded at different azimuthal angles (φ) at high energy ($E = 7.5$ keV). Note the dramatic influence of a very small azimuthal misalignment on the resulting GISAXS image.

3.3. Fourier transform holography

The inset in Fig. 7 shows the Fourier transform hologram (FTH) on a logarithmic scale from a 1 μm sample (CoPd film deposited on a 150 μm -thick Si_3N_4 membrane) and three reference holes of about 100 nm. It is important to stress that we were interested here in implementing a FTH geometry of the MagSAXS set-up on the SEXTANTS beamline at Synchrotron SOLEIL. For that purpose we measured a test sample belonging to a set obtained during the focused-ion-beam (FIB) milling process optimization, for different exposure times and doses, similar to the one presented by Eisebitt *et al.* (2004) and Streit-Nierobisch *et al.* (2009). We may highlight two main advantages in our approach, using a scintillator and a visible-light CCD instead of the directly illuminated CCDs (Streit-Nierobisch *et al.*, 2009). Firstly, the alignment procedure is straightforward since the detection system does not suffer from saturation by the direct beam transmitted through the sample. Therefore the sample can be easily found by overexposing the CCD camera. Secondly, no beam-stop nor fast shutter system are used (Eisebitt *et al.*, 2004; Streit-Nierobisch *et al.*, 2009). In this way the FTH scheme is lighter and allows a more flexible experimental set-up. Moreover, the beam-stop and the beam-stop holder contributions no longer have to be subtracted or cleaned from the Fourier-transformed hologram in the real-images retrieval process (Streit-Nierobisch *et al.*, 2009).

Holograms were recorded at the Co L_3 -edge for two opposite helicities of the circularly polarized X-ray photons. Even though no magnetic contrast could be shown, our

approach shows how this optical-based FTH set-up can be used. Several exposure times were tested in order to check the limits of detection. For the lowest limit an exposure time of 5 min was used, allowing enough contrast to observe the interference between the sample and the reference holes without saturating the central part. The larger exposure time used was 60 min, a value compatible with respect to the SEXTANTS beamline stability and sample drifts. Since we found that the contrast obtained after 15 min exposure time was similar to the 60 min exposure time, several 15 min images were recorded and summed afterwards (Fig. 7, the centered inset shows the sum of 31 images). The recorded hologram presents well defined interference coming from the sample itself and the three reference holes. A static speckle distribution can also be clearly observed. The two strikes crossing in the central part are probably due to sample borders interferences. Fig. 7 shows the resulting Fourier-transformed hologram of the log-scaled CCD summed image. The saturated central part of the image was not removed to perform the Fourier transform. We may stress here that in order to obtain the real shape of the central part we can record an image without saturating this part and then just replace it after scaling in the final hologram. In this way the fine circular interferences can be removed from the Fourier-transformed hologram. The three reference holes produce six real-space images: the reconstructed image, A , as well as its complex conjugate, A^* , rotated by 180° , multiplied by the three-fold symmetry. Increased statistics, *i.e.* increased number of images contributing in the final summation, would improve the data quality. Owing to the long exposure times, time-resolved experiments cannot be envisaged using the MagSAXS set-up applied for the FTH experiments. The set-up is intended to be used complementarily to the direct illuminated CCD set-up, allowing, for example, pre-alignment and/or transmission measurements.

4. Conclusions

In summary, we have described a new set-up and demonstrated the usefulness of using a visible-light optical-based image-transport set-up for resonant soft X-ray magnetic scattering. A YAG:Ce scintillator is used to collect the scattered X-ray beam and convert it to visible light, which is then recorded by a CCD camera placed outside the constraining sample environment (UHV, high magnetic field, very low temperature). Very good quality data are obtained both for charge and magnetic scattering contrasts, with reasonable exposure times, *i.e.* a few seconds. A full dataset characterizing the magnetic properties of a Co grating was recorded as a function of energy and for different q by integrating the diffuse magnetic scattering orders. Their evolution with respect to photon energy shows features similar to those obtained using zero- or one-dimensional detectors in down-graded sample conditions. Magnetic structure factor calculations are necessary to completely reproduce the complex charge–charge, magnetic–magnetic and crossed charge–magnetic interferences. We have shown that the MagSAXS

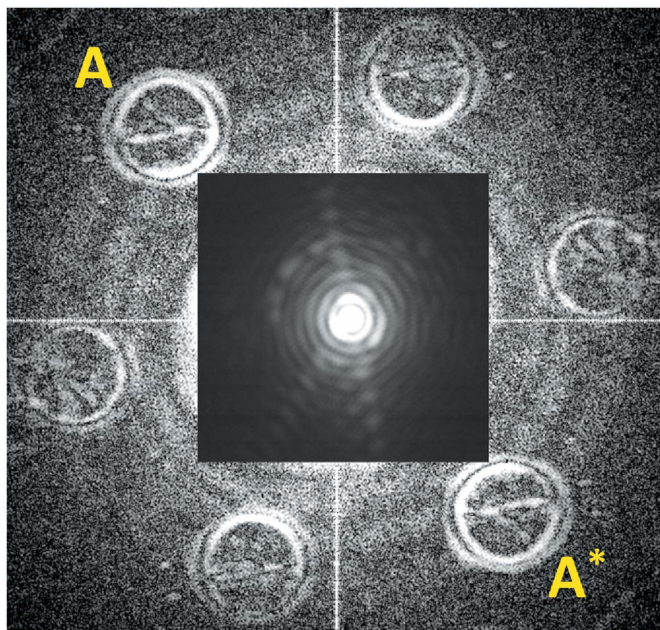


Figure 7 Fourier transform holography diagram obtained from the sample with three reference pinholes (see details in the text). Six real-space images can be observed: the reconstructed image, A , as well as its complex conjugate, A^* , rotated by 180° , multiplied by the three-fold symmetry. The inset shows the sum of 31 images recorded with an exposure time of 15 min each.

set-up can be used easily for hard X-ray GISAXS measurements. We have shown the high sensitivity of the collected scattered orders with the azimuth misalignment. Finally, the MagSAXS set-up is a viable, safe and cheap option for high-sensitivity FTH magnetostatic experiments.

We acknowledge the financial support from the RTRA ‘Triangle de la Physique’ under grant number 2010-014T. We want to thank Pascal Mercere from METROLOGIE, Fadi Choueikani from DEIMOS, and Nicolas Jaouen and Horia Popescu from SEXTANTS beamlines for their help during the experiments. We acknowledge the help of Adrien Besson for the SEM measurements. Sufal Swaraj is acknowledged for a critical reading of the manuscript and François Montaigne from the Laboratoire de Physique des Matériaux of Nancy, France, for providing the nanoimprinted sample. The SOLEIL synchrotron facility is acknowledged for providing the beam time.

References

- Beutier, G., Marty, A., Livet, F., van der Laan, G., Stanescu, S. & Bencok, P. (2007). *Rev. Sci. Instrum.* **78**, 093901.
- Beutier, G., van der Laan, G., Marty, A. & Livet, F. (2008). *Eur. Phys. J. Appl. Phys.* **42**, 161–167.
- Bras, W. (2007). *J. Appl. Cryst.* **40**, s52–s56.
- Brune, H. & Gambardella, P. (2009). *Surf. Sci.* **603**, 1812–1830.
- Chesnel, K., Belakhovsky, M., Landis, S., Toussaint, J. C., Collins, S. P., van der Laan, G., Dudzik, E. & Dhesi, S. S. (2002). *Phys. Rev. B*, **66**, 024435.
- Chou, S. Y., Krauss, P. R. & Renstrom, P. J. (1996). *Science*, **272**, 85–87.
- CRYTUR (2012). *CRYTUR YAG:Ce*, <http://www.crytur.cz/pages/25/YAG:Ce>.
- Dürr, H. A., Dudzik, E., Dhesi, S. S., Goedkoop, J. B., van der Laan, G., Belakhovsky, M., Mocuta, C., Marty, A. & Samson, Y. (1999). *Science*, **284**, 2166–2168.
- Eerenstein, W., Mathur, N. D. & Scott, J. F. (2006). *Nature (London)*, **442**, 759–765.
- Eisebitt, S., Lüning, J., Schlotter, W. F., Lörger, M., Hellwig, O., Eberhardt, W. & Stöhr, J. (2004). *Nature (London)*, **432**, 885–888.
- Fischer, P., Zeller, R., Schütz, G., Goerigk, G. & Haubold, H.-G. (1997). *J. Phys.* **IV**, **7**, C2-753–C2-755.
- Hellwig, O., Margulies, D. T., Lengsfeld, B., Fullerton, E. E. & Kortright, J. B. (2002). *Appl. Phys. Lett.* **80**, 1234–1236.
- Kao, C. C., Chen, C. T., Johnson, E. D., Hastings, J. B., Lin, H. J., Ho, G. H., Meigs, G., Brot, J. M., Hulbert, S. L., Idzerda, Y. U. & Vettier, C. (1994). *Phys. Rev. B*, **50**, 9599–9602.
- Kao, C. C., Hastings, J. B., Johnson, E. D., Siddons, D. P., Smith, G. C. & Prinz, G. A. (1990). *Phys. Rev. Lett.* **65**, 373–376.
- Kortright, J. B., Hellwig, O., Margulies, D. T. & Fullerton, E. E. (2001a). *J. Magn. Magn. Mater.* **240**, 325–330.
- Kortright, J. B., Kim, S. K., Denbeau, G. P., Zeltzer, G., Takano, K. & Fullerton, E. E. (2001b). *Phys. Rev. B*, **64**, 092401.
- Laan, G. van der (2008). *C. R. Phys.* **9**, 570–584.
- Miguel, J., Camarero, J., Vogel, J., Peters, J. F., Brookes, N. B. & Goedkoop, J. (2007). *Appl. Surf. Sci.* **254**, 335–338.
- Miguel, J., Peters, J. F., Toulemonde, O. M., Dhesi, S. S., Brookes, N. B. & Goedkoop, J. B. (2006). *Phys. Rev. B*, **74**, 094437.
- Moubah, R., Elzo, M., Moussaoui, S. E., Colson, D., Jaouen, N., Belkhou, R. & Viret, M. (2012). *Appl. Phys. Lett.* **100**, 042406.
- Optique Peter (2012). *OPTIQUE PETER*, <http://www.optiquepeter.com/en/index.php>.
- PCO2000 (2012). *PCEO Sensitive Cameras*, <http://www.pco.de/sensitive-cameras/pco2000/>.
- Peters, J. F., Miguel, J., de Vries, M. A., Toulemonde, O. M., Goedkoop, J., Dhesi, S. S. & Brookes, N. B. (2004). *Phys. Rev. B*, **70**, 224417.
- Renaud, G., Lazzari, R. & Leroy, F. (2009). *Surf. Sci. Rep.* **64**, 255–380.
- Saavedra, H. M., Mullen, T. J., Zhang, P., Dewey, D. C., Claridge, S. A. & Weiss, P. S. (2010). *Rep. Prog. Phys.* **73**, 036501.
- Seemann, K. M., Garcia-Sanchez, F., Kronast, F., Miguel, J., Kakay, A., Schneider, C. M. & Hertel, R. (2012). *Phys. Rev. Lett.* **108**, 077201.
- Skuzza, J. R., Clavero, C., Yang, K., Wincheski, B. & Lukaszew, R. A. (2010). *IEEE Trans. Magn.* **46**, 1886–1889.
- Spezzani, C., Torelli, P., Delaunay, R., Hague, C. F., Petroff, F., Scholl, A., Gullikson, E. M. & Sacchi, M. (2004). *Physica B*, **345**, 153–156.
- Streit-Nierobisch, S., Stickler, D., Gutt, C., Stadler, L.-M., Stillrich, H., Menk, C., Frömter, R., Tieg, C., Leupold, O., Oepen, H. P. & Grübel, G. (2009). *J. Appl. Phys.* **106**, 083909.
- Tonnerre, J. M., Sève, L., Raoux, D., Soullié, G., Rodmacq, B. & Wolfers, P. (1995). *Phys. Rev. Lett.* **75**, 740–743.
- Yan, M. & Gibaud, A. (2007). *J. Appl. Cryst.* **40**, 1050–1055.